Advances in Materials Research, *Vol. 15, No. 2 (2026) 125-144*
https://doi.org/10.12989/amr.2026.15.2.125

Techno-Press

Optimization and fabrication cost management of GPL reinforcement's geometry via a semi-analytical approach

Suleiman Ibrahim Mohammad*[1,2], Asokan Vasudevan[3], Basem Abu Zneid[4], Torki M. Al-Fawwaz[5], Wu Wenya[6,7], Ismoiljon Rozikov[8], Fakhriddin Isaev[9,10], Alisher Ishankulov[11]

[1]*Electronic Marketing and Social Media, Economic and Administrative Sciences Zarqa University, Jordan*
[2]*INTI International University, 71800 Negeri Sembilan, Malaysia*
[3]*Faculty of Business and Communications, INTI International University, 71800 Negeri Sembilan, Malaysia*
[4]*Faculty of Engineering, Hourani Center for Applied Scientific Research, Al-Ahliyya Amman University, Amman, Jordan*
[5]*College of Commerce and Business, Lusail University, Qatar*
[6]*Xingtai Vocational College of Applied Technology, Hebei Province, China*
[7]*INTI International University, 71800 Negeri Sembilan, Malaysia*
[8]*Department of Agronomy Navoi State University of Mining and Technologies, Navoiy, Uzbekistan*
[9]*Department of Finance and Tourism, Termez University of Economics and Service, Termez, Uzbekistan*
[10]*Research Center CEDR under the Tashkent State University of Economics, Tashkent, Uzbekistan*
[11]*Department of Chemistry, Kimyo International University in Tashkent Branch Samarkand, Uzbekistan*

(Received October 21, 2025, Revised March 26, 2026, Accepted April 6, 2026)

Abstract. A semi-analytical framework has been outlined in order to determine optimal costs for both graphite enhance composite structures and to manage the fabrication/production cost reduction of each composite component subjected to an outside/acting shock load (dynamic). The mechanical behavior of the composite (the composite composite system) will be simulated/characterized by means of Halpin-Tsai theory to find out what the effective material properties will be based upon the shape/geometry of the graphene nanoplatelet (GPL) within the composite (shape). Structural outputs will be computed using first-order-shear-deformation-theory (FSDT) in order for each composite block of the frame to accurately reflect transverse shear effects that result from moderate thicknesses of the plates under load (weight). Hamilton's principle will steer the development of the governing equations of motion for each of the composite blocks to develop analytical representations (the 2D composite) of their (combination) response when they are loaded with a transient shock/impact. Coupled partial differential equations will be solved using the differential quadrature method (DQM) semi-analytically to provide the highest degree of accuracy, while also minimizing the amount of computational effort through reduced discretization methods required to solve them. Finally, time-dependent shock loading or transient response solutions will be obtained using the Laplace transformations. This work is unique because it integrates geometric optimization of the nanoplates with a manufacturing cost-reduction assessment to find the best performing solutions with the least manufacturing cost.

Keywords: differential quadrature method; external shock; GPL reinforcement; optimization and fabrication cost management; structural responses

*Corresponding author, Ph.D., E-mail: dr_sliman@yahoo.com

Copyright © 2026 Techno-Press
http://www.techno-press.org/amr/5
ISSN: 2234-0912 (Print), 2234-179X (Online)

1. Introduction

Geotechnical and structural engineers increasingly rely on advanced reinforcement methods to enhance the performance and durability of soil and foundation systems [1]. Among these methods, GPL reinforcement has emerged as a critical technique for improving load-bearing capacity and stability [2]. By integrating high-strength polymer-based materials into soil structures, engineers can effectively mitigate issues such as settlement, erosion, and slope failure [3]. The importance of GPL reinforcement lies in its ability to distribute stresses more uniformly, thereby reducing localized weaknesses within the soil mass [4]. Furthermore, it offers a cost-effective and sustainable alternative to traditional reinforcement techniques, minimizing the need for excessive excavation or high-volume material use [5]. In infrastructure projects such as roads, retaining walls, and embankments, GPL systems significantly enhance long-term performance and resilience [6]. Engineers also benefit from the adaptability of GPL materials, which can be tailored to suit varying environmental and loading conditions [7]. The technique contributes to improved safety margins, particularly in regions prone to seismic activity or extreme weather events [8]. Additionally, GPL reinforcement aligns with modern engineering practices that emphasize sustainability and resource efficiency [9]. Therefore, understanding and applying GPL reinforcement principles is essential for engineers aiming to design robust, efficient, and future-ready infrastructure systems [10].

Stability analysis is a fundamental aspect of engineering that ensures the safety and reliability of structures and systems under various loading conditions [11]. It involves evaluating whether a structure can maintain its equilibrium without experiencing failure, excessive deformation, or collapse [12]. Engineers across disciplines, including civil, mechanical, and aerospace engineering, rely on stability analysis to design structures that can withstand both expected and unforeseen forces [13]. The importance of this analysis lies in its ability to predict potential failure modes before construction or implementation [14]. By identifying critical load thresholds, engineers can incorporate appropriate safety factors into their designs [15]. Stability analysis is particularly essential in the design of slopes, foundations, retaining walls, and tall structures, where instability can lead to catastrophic consequences [16]. It also plays a key role in understanding phenomena such as buckling, which can occur in slender structural elements under compressive loads [17]. Advanced computational tools and numerical methods have significantly improved the accuracy and efficiency of stability assessments [18]. These tools enable engineers to simulate complex interactions between materials, geometry, and external forces [19]. Furthermore, stability analysis contributes to optimizing material usage, reducing costs while maintaining safety standards [20]. In geotechnical engineering, it helps assess soil behavior and prevent landslides or ground failures [21]. In structural engineering, it ensures that buildings and bridges remain secure under dynamic loads such as wind and earthquakes [22]. The integration of stability analysis into the design process enhances the overall resilience and durability of infrastructure systems [23]. It also supports compliance with engineering codes, standards, and regulatory requirements [24]. Ultimately, a thorough understanding of stability analysis is indispensable for engineers striving to develop safe, efficient, and sustainable solutions in modern engineering practice [25].

A comprehensive semi-analytical methodology is developed to investigate the optimization and fabrication cost efficiency of graphene nanoplatelet-reinforced composite structures under external shock loading. The effective elastic properties of the nanocomposite are evaluated using the Halpin–Tsai model, explicitly incorporating the influence of nanoplatelet geometry, aspect ratio, and dispersion characteristics. Structural behavior is formulated within the framework of FSDT,

allowing accurate prediction of shear deformation effects in thick plate configurations. The governing equations of motion are systematically derived via Hamilton's principle, capturing the dynamic response of the system subjected to transient shock excitation. To solve the resulting equations, the DQM is employed as a powerful semi-analytical tool, providing high precision with minimal computational cost. The Laplace transform technique is further integrated to efficiently address time-domain shock loading and obtain closed-form or rapidly convergent solutions. In addition to mechanical analysis, this study emphasizes fabrication cost management by correlating GNP geometrical parameters with manufacturing complexity and material usage. A parametric optimization scheme is introduced to identify configurations that maximize stiffness and impact resistance while minimizing production costs. The results demonstrate that strategic control of nanoplatelet geometry and distribution leads to significant improvements in dynamic performance without proportional increases in fabrication expenses. The proposed approach offers a unified framework for design optimization and cost-effective manufacturing of advanced graphene-reinforced composites, making it highly applicable to aerospace, automotive, and protective structural systems where performance under shock loading is critical.

2. Problem formulation

Throughout the plate's thickness, the graphene platelet reinforcements are uniformly dispersed and functionally graded. Their distribution is defined mathematically by the following expressions.

$$\text{GNP-X: } \mathfrak{v}_{GNP}(\mathfrak{f}) = 4\left(\frac{|\mathfrak{z}_{\mathfrak{f}}|}{h^c}\right)\mathfrak{v}_{GNP}^T \tag{1a}$$

$$\text{GNP-O: } \mathfrak{v}_{GNP}(\mathfrak{f}) = \left(2 - 4\left(\frac{|\mathfrak{z}_{\mathfrak{f}}|}{h^c}\right)\right)\mathfrak{v}_{GNP}^T \tag{1b}$$

$$\text{GNP-UD: } \mathfrak{v}_{GNP}(\mathfrak{f}) = \mathfrak{v}_{GNP}^T \tag{1c}$$

where $\mathfrak{z}_{\mathfrak{f}} = -\frac{h^c}{2} + \frac{k-1}{N_L-1}h^c, \mathfrak{f} = 1, \dots, N_L, h$ is the total thickness and $\mathfrak{v}_{GNP}^T$ is the overall reinforcement volume %. The volume fraction may be obtained using the following formula:

$$\mathfrak{v}_{GNP}^T = \frac{1}{1+(\frac{\rho_{GNP}}{\rho_M})(\frac{1}{W_{GNP}}-1)}. \tag{2}$$

where W_{GNP} is the weight percentage and ρ is the density. The effective Young's modulus of the nanocomposite may be predicted using the Halpin-Tsai model.

$$\mathbb{E}^{(k)}(\mathfrak{z}) = 0.49\mathbb{E}_l + 0.51\mathbb{E}_t. \tag{3}$$

When the following formula is used to get the longitudinal and transverse moduli:

$$\mathbb{E}_l = \frac{\mathbb{E}_M(1+\mathbb{a}_l\mathbb{b}_l\mathfrak{v}_{GNP})}{1-\mathfrak{v}_{GNP}\mathbb{a}_l}, \mathbb{a}_l = \frac{\left(\frac{\mathbb{E}_{GNP}}{\mathbb{E}_M}\right)-1}{\left(\frac{\mathbb{E}_{GNP}}{\mathbb{E}_M}\right)+\xi_l}, \text{ and } \mathbb{a}_t = \frac{\left(\frac{\mathbb{E}_{GNP}}{\mathbb{E}_M}\right)-1}{\left(\frac{\mathbb{E}_{GNP}}{\mathbb{E}_M}\right)+\xi_t} \tag{4a}$$

$$\mathbb{E}_t = \frac{\mathbb{E}_M(1+\mathbb{a}_t\,\mathbb{b}_t\mathfrak{v}_{GNP})}{1-\mathfrak{v}_{GNP}\,\mathbb{a}_t}. \tag{4b}$$

where $\mathbb{E}_{GNP}$ is the elastic modulus of the reinforcement and ξ_l and ξ_t are geometry factors. The parameters ξ_l and ξ_t characterise the size and form of naofillers.

$$\mathbb{b}_l = \mathbb{b}_t = \frac{2d_{GNP}}{h_{GNP}}. \tag{5}$$

where the thickness and diameter of the reinforcement phase are denoted by d_{GNP} and h_{GNP}, respectively. The rule of mixing may be used to get the core's effective Poisson's ratio.

$$\nu^{(k)}(\mathfrak{z}) = \nu_M \mathfrak{v}_M + \nu_{GNP} \mathfrak{v}_{GNP}. \tag{6a}$$

where ν_M and ν_{GNP} are the matrix and reinforcement Poisson's ratios, respectively. The law of mixing may be used to calculate the core's effective density.

$$\rho^{(k)}(\mathfrak{z}) = \rho_M \mathfrak{v}_M + \rho_{GNP} \mathfrak{v}_{GNP}. \tag{6b}$$

Poisson's ratio and this use the same approach. The effective shear modulus of the composite may be computed using the following formula.

$$G_{eff} = \frac{G_{upper} + G_{lower}}{2}. \tag{6c}$$

In which

$$G_{upper} = \mathfrak{v}_M G_M + \mathfrak{v}_{GNP} G_{GNP} \tag{6d}$$

$$G_{lower} = \left(\frac{\mathfrak{v}_M}{G_M} + \frac{\mathfrak{v}_{GNP}}{G_{GNP}}\right)^{-1}. \tag{6e}$$

2.1 Displacement field

We describe the kinematic field of the structure using the first order shear deformation theory (FSDT), which was previously covered in the introduction.

$$\begin{aligned} \mathfrak{u}(\mathfrak{r}, \theta, \mathfrak{z}, \mathfrak{t}) &= \mathfrak{u}_0(\mathfrak{r}, \theta, \mathfrak{t}) + \mathfrak{z}\mathfrak{u}_1(\mathfrak{r}, \theta, \mathfrak{t}), \\ \mathfrak{v}(\mathfrak{r}, \theta, \mathfrak{z}, \mathfrak{t}) &= \mathfrak{v}_0(\mathfrak{r}, \theta, \mathfrak{t}) + \mathfrak{z}\mathfrak{v}_1(\mathfrak{r}, \theta, \mathfrak{t}), \\ \mathfrak{w}(\mathfrak{r}, \theta, \mathfrak{z}, \mathfrak{t}) &= \mathfrak{w}_0(\mathfrak{r}, \theta, \mathfrak{t}). \end{aligned} \tag{7}$$

This is how the strain displacement is explained.

$$\mathfrak{E}_{\mathfrak{r}\mathfrak{r}} = \frac{\partial \mathfrak{u}_0}{\partial \mathfrak{r}} + \mathfrak{z}\frac{\partial \mathfrak{u}_1}{\partial \mathfrak{r}}, \tag{8a}$$

$$\mathfrak{E}_{\theta\theta} = \frac{1}{\mathfrak{r}}\left(\mathfrak{u}_0 + \mathfrak{z}\mathfrak{u}_1 + \frac{\partial \mathfrak{v}_0}{\partial \theta} + \mathfrak{z}\frac{\partial \mathfrak{v}_1}{\partial \theta}\right), \tag{8b}$$

$$\mathfrak{E}_{\mathfrak{z}\mathfrak{z}} = \mathfrak{w}_1, \tag{8c}$$

$$\mathfrak{E}_{\mathfrak{r}\mathfrak{z}} = \mathfrak{u}_1 + \frac{\partial \mathfrak{w}_0}{\partial \mathfrak{r}}, \tag{8d}$$

$$\mathfrak{E}_{\mathfrak{r}\theta} = \frac{1}{\mathfrak{r}}\left(\frac{\partial \mathfrak{u}_0}{\partial \theta} + \mathfrak{z}\frac{\partial \mathfrak{u}_1}{\partial \theta}\right) + \frac{\partial \mathfrak{v}_0}{\partial \mathfrak{r}} + \mathfrak{z}\frac{\partial \mathfrak{v}_1}{\partial \mathfrak{r}} - \frac{1}{\mathfrak{r}}(\mathfrak{v}_0 + \mathfrak{z}\mathfrak{v}_1), \tag{8e}$$

$$\mathfrak{E}_{\theta\mathfrak{z}} = \mathfrak{v}_1 + \frac{1}{\mathfrak{r}}\left(\frac{\partial \mathfrak{w}_0}{\partial\theta}\right), \tag{8f}$$

For the chosen mechanical, we have also incorporated the following fundamental relations:

$$\begin{Bmatrix} \mathfrak{T}_{\mathfrak{rr}} \\ \mathfrak{T}_{\theta\theta} \\ \mathfrak{T}_{\mathfrak{z}\mathfrak{z}} \\ \mathfrak{T}_{\theta\mathfrak{z}} \\ \mathfrak{T}_{\mathfrak{r}\mathfrak{z}} \\ \mathfrak{T}_{\mathfrak{r}\theta} \end{Bmatrix} = \begin{bmatrix} \mathfrak{P}_{11} & \mathfrak{P}_{12} & \mathfrak{P}_{13} & 0 & 0 & 0 \\ \mathfrak{P}_{21} & \mathfrak{P}_{22} & \mathfrak{P}_{23} & 0 & 0 & 0 \\ \mathfrak{P}_{31} & \mathfrak{P}_{32} & \mathfrak{P}_{33} & 0 & 0 & 0 \\ 0 & 0 & 0 & \mathfrak{P}_{44} & 0 & 0 \\ 0 & 0 & 0 & 0 & \mathfrak{P}_{55} & 0 \\ 0 & 0 & 0 & 0 & 0 & \mathfrak{P}_{66} \end{bmatrix} \begin{Bmatrix} \mathfrak{E}_{\mathfrak{rr}} \\ \mathfrak{E}_{\theta\theta} \\ \mathfrak{E}_{\mathfrak{z}\mathfrak{z}} \\ \mathfrak{E}_{\theta\mathfrak{z}} \\ \mathfrak{E}_{\mathfrak{r}\mathfrak{z}} \\ \mathfrak{E}_{\mathfrak{r}\theta} \end{Bmatrix}, \tag{9}$$

In which [26-28]

$$\begin{gathered} \mathfrak{P}_{11} = \frac{E_c(1-\nu_c)}{(1+\nu_c)(1-2\nu_c)}, \mathfrak{P}_{33} = \mathfrak{P}_{22} = \mathfrak{P}_{11}, \mathfrak{P}_{12} = \frac{E_c\nu_c}{(1+\nu_c)(1-2\nu_c)}, \\ \mathfrak{P}_{13} = \mathfrak{P}_{23} = \mathfrak{P}_{12}, \mathfrak{P}_{44} = \frac{E_c}{2(1+\nu_c)}, \mathfrak{P}_{66} = \mathfrak{P}_{55} = \mathfrak{P}_{44}. \end{gathered} \tag{10}$$

2.2 Hamilton's principle

The basic equations of our study are placed in the variational energy configuration shown below using Hamilton's principle [29].

$$\int_{\mathfrak{t}_1}^{\mathfrak{t}_2}\left(\delta\Pi_k - (\delta\Pi_e - \delta\Pi_{\mathfrak{w}})\right)d\mathfrak{t} = 0, \tag{11}$$

The aforementioned parameters are shown by the following formulae.

$$\Pi_k = \int \rho_c \left[\left(\frac{\partial \mathfrak{u}}{\partial \mathfrak{t}}\right)^2 + \left(\frac{\partial \mathfrak{v}}{\partial \mathfrak{t}}\right)^2 + \left(\frac{\partial \mathfrak{w}}{\partial \mathfrak{t}}\right)^2\right] dV, \tag{12a}$$

$$\Pi_e = \int\left\{\mathfrak{T}_{\mathfrak{rr}}\mathfrak{E}_{\mathfrak{rr}} + \mathfrak{T}_{\theta\theta}\mathfrak{E}_{\theta\theta} + \mathfrak{T}_{\mathfrak{z}\mathfrak{z}}\mathfrak{E}_{\mathfrak{z}\mathfrak{z}} + \mathfrak{T}_{\theta\mathfrak{z}}\mathfrak{E}_{\theta\mathfrak{z}} + \mathfrak{T}_{\mathfrak{r}\mathfrak{z}}\mathfrak{E}_{\mathfrak{r}\mathfrak{z}} + \mathfrak{T}_{\mathfrak{r}\theta}\mathfrak{E}_{\mathfrak{r}\theta}\right\}dV, \tag{12b}$$

The external shock on the system, denoted as $P(\mathfrak{r},\theta,\mathfrak{t})$, is used to compute the external work, $\Pi_{\mathfrak{w}}$.

$$\Pi_{\mathfrak{w}} = \int_A PH(\mathfrak{t}-\mathfrak{t}_0)\mathfrak{w}_0 dA. \tag{13}$$

The equations below were created by modifying Eq. (11) to include Eqs. (12a-b, 13).

$$\delta\mathfrak{u}_0 \quad : \quad \frac{1}{\mathfrak{r}}\frac{\partial(\mathfrak{r}\mathbb{m}_{\mathfrak{rr}})}{\partial\mathfrak{r}} - \frac{\mathbb{m}_{\theta\theta}}{\mathfrak{r}} + \frac{\partial\mathbb{m}_{\mathfrak{r}\theta}}{\mathfrak{r}\partial\theta} = \mathfrak{f}_0\ddot{\mathfrak{u}}_0 + \mathfrak{f}_1\ddot{\mathfrak{u}}_1, \tag{14a}$$

$$\delta\mathfrak{v}_0 \quad : \quad \frac{1}{\mathfrak{r}}\frac{\partial\mathbb{m}_{\theta\theta}}{\partial\theta} + \frac{1}{\mathfrak{r}}\frac{\partial(\mathfrak{r}\mathbb{m}_{\mathfrak{r}\theta})}{\partial\mathfrak{r}} + \frac{\mathbb{m}_{\mathfrak{r}\theta}}{\mathfrak{r}} = \mathfrak{f}_0\ddot{\mathfrak{v}}_0 + \mathfrak{f}_1\ddot{\mathfrak{v}}_1, \tag{14b}$$

$$\delta\mathfrak{w}_0 \quad : \quad \frac{1}{\mathfrak{r}}\frac{\partial\mathbb{m}_{\theta\mathfrak{z}}}{\partial\theta} + \frac{1}{\mathfrak{r}}\frac{\partial(\mathfrak{r}\mathbb{m}_{\mathfrak{r}\mathfrak{z}})}{\partial\mathfrak{r}} - PH(\mathfrak{t}-\mathfrak{t}_0) - \mathbb{m}^T\nabla^2\mathfrak{w}_0 = \mathfrak{f}_0\ddot{\mathfrak{w}}_0, \tag{14c}$$

$$\delta\mathfrak{u}_1 \quad : \quad \frac{1}{\mathfrak{r}}\frac{\partial(\mathfrak{r}\mathbb{m}_{\mathfrak{rr}})}{\partial\mathfrak{r}} - \frac{\mathbb{m}_{\theta\theta}}{\mathfrak{r}} + \frac{\partial\mathbb{m}_{\mathfrak{r}\theta}}{\mathfrak{r}\partial\theta} - \mathbb{m}_{\mathfrak{r}\mathfrak{z}} = \mathfrak{f}_1\ddot{\mathfrak{u}}_0 + \mathfrak{f}_2\ddot{\mathfrak{u}}_1, \tag{14d}$$

$$\delta \mathfrak{v}_1 \quad : \quad \frac{1}{\mathfrak{r}}\frac{\partial \mathbb{m}_{\theta\theta}}{\partial \theta} + \frac{1}{\mathfrak{r}}\frac{\partial (\mathfrak{r}\mathbb{m}_{\mathfrak{r}\theta})}{\partial \mathfrak{r}} + \frac{\mathbb{m}_{\mathfrak{r}\theta}}{\mathfrak{r}} - \mathbb{m}_{\theta\mathfrak{z}} = \mathfrak{f}_1 \ddot{\mathfrak{v}}_0 + \mathfrak{f}_2 \ddot{\mathfrak{v}}_1, \tag{14e}$$

The matching boundary conditions are described as

$$\begin{aligned}
&\delta \mathfrak{u}_0: \quad \mathbb{m}_{\mathfrak{r}\mathfrak{r}}\hat{n}_{\mathfrak{r}} + \frac{\mathbb{m}_{\mathfrak{r}\theta}}{\mathfrak{r}}\hat{n}_{\theta} = 0,\\
&\delta \mathfrak{v}_0: \quad \mathbb{m}_{\mathfrak{r}\theta}\hat{n}_{\mathfrak{r}} + \frac{\mathbb{m}_{\theta\theta}}{\mathfrak{r}}\hat{n}_{\theta} = 0,\\
&\delta \mathfrak{w}_0: \quad \mathbb{m}_{\mathfrak{r}\mathfrak{z}}\hat{n}_{\mathfrak{r}} + \frac{\mathbb{m}_{\theta\mathfrak{z}}}{\mathfrak{r}}\hat{n}_{\theta} = 0,\\
&\delta \mathfrak{u}_1: \quad \mathbb{mm}_{\mathfrak{r}\mathfrak{r}}\hat{n}_{\mathfrak{r}} + \frac{\mathbb{mm}_{\mathfrak{r}\theta}}{\mathfrak{r}}\hat{n}_{\theta} = 0,\\
&\delta \mathfrak{v}_1: \quad \mathbb{mm}_{\mathfrak{r}\theta}\hat{n}_{\mathfrak{r}} + \frac{\mathbb{mm}_{\theta\theta}}{\mathfrak{r}}\hat{n}_{\theta} = 0,
\end{aligned} \tag{15}$$

where:

$$\begin{aligned}
&\mathbb{m}_{\mathfrak{r}\mathfrak{r}} = \int_V (\mathfrak{T}_{\mathfrak{r}\mathfrak{r}})\mathfrak{r}d\mathfrak{r}d\theta d\mathfrak{z}\,, \mathbb{mm}_{\mathfrak{r}\mathfrak{r}} = \int_V (\mathfrak{z}\mathfrak{T}_{\mathfrak{r}\mathfrak{r}})\mathfrak{r}d\mathfrak{r}d\theta d\mathfrak{z},\\
&\mathbb{m}_{\theta\theta} = \int_V (\mathfrak{T}_{\theta\theta})\mathfrak{r}d\mathfrak{r}d\theta d\mathfrak{z},\ \mathbb{mm}_{\theta\theta} = \int_V (\mathfrak{z}\mathfrak{T}_{\theta\theta})\mathfrak{r}d\mathfrak{r}d\theta d\mathfrak{z},\\
&\mathbb{m}_{\mathfrak{z}\mathfrak{z}} = \int_V \left(\mathfrak{T}_{\mathfrak{z}\mathfrak{z}}\right)\mathfrak{r}d\mathfrak{r}d\theta d\mathfrak{z},\ \mathbb{mm}_{\mathfrak{z}\mathfrak{z}} = \int_V \left(\mathfrak{z}\mathfrak{T}_{\mathfrak{z}\mathfrak{z}}\right)\mathfrak{r}d\mathfrak{r}d\theta d\mathfrak{z},\\
&\mathbb{m}_{\theta\mathfrak{z}} = \int_V \left(\mathfrak{T}_{\theta\mathfrak{z}}\right)\mathfrak{r}d\mathfrak{r}d\theta d\mathfrak{z},\ \mathbb{mm}_{\theta\mathfrak{z}} = \int_V \left(\mathfrak{z}\mathfrak{T}_{\theta\mathfrak{z}}\right)\mathfrak{r}d\mathfrak{r}d\theta d\mathfrak{z},\\
&\mathbb{m}_{\mathfrak{r}\mathfrak{z}} = \int_V \left(\mathfrak{T}_{\mathfrak{r}\mathfrak{z}}\right)\mathfrak{r}d\mathfrak{r}d\theta d\mathfrak{z},\ \mathbb{mm}_{\mathfrak{r}\mathfrak{z}} = \int_V \left(\mathfrak{z}\mathfrak{T}_{\mathfrak{r}\mathfrak{z}}\right)\mathfrak{r}d\mathfrak{r}d\theta d\mathfrak{z},\\
&\mathbb{m}_{\mathfrak{r}\theta} = \int_V (\mathfrak{T}_{\mathfrak{r}\theta})\mathfrak{r}d\mathfrak{r}d\theta d\mathfrak{z},\ \mathbb{mm}_{\mathfrak{r}\theta} = \int_V (\mathfrak{z}\mathfrak{T}_{\mathfrak{r}\theta})\mathfrak{r}d\mathfrak{r}d\theta d\mathfrak{z},\\
&\{\mathfrak{f}_0, \mathfrak{f}_1, \mathfrak{f}_2, \mathfrak{f}_3, \mathfrak{f}_4, \mathfrak{f}_5, \mathfrak{f}_6\} = \int_V (\{1, \mathfrak{z}, \mathfrak{z}^2, \mathfrak{z}^3, \mathfrak{z}^4, \mathfrak{z}^5, \mathfrak{z}^6\}\rho_c)\mathfrak{r}d\mathfrak{r}d\theta d\mathfrak{z}.
\end{aligned} \tag{16}$$

3. Solution using a semi-analytical approach

The main procedures for obtaining a numerical solution using the DQA are described in this section.

3.1 Differential quadrature approach

The $\mathfrak{p}^{th}$ derivative of a one-dimensional function may be obtained using the DQA concepts as [30].

$$\frac{\partial^{\mathfrak{p}} \mathbb{F}(\mathfrak{r})}{\partial \mathfrak{r}^{\mathfrak{p}}} = \sum_{\mathfrak{j}=1}^{\mathfrak{n}_{\mathfrak{r}}} \mathfrak{a}_{\mathfrak{s}\mathfrak{j}}^{(\mathfrak{p})} \mathfrak{o}(\mathfrak{r}_{\mathfrak{j}})\ for\ \mathfrak{s} = 1,2,\ldots,\mathfrak{n}_{\mathfrak{r}}\ and\ \mathfrak{p} = 1,2,\ldots,\mathfrak{n}_{\mathfrak{r}} - 1. \tag{17}$$

Here, $\mathfrak{a}_{\mathfrak{s}\mathfrak{j}}^{(\mathfrak{p})}$ denotes the weight coefficients for the $\mathfrak{s}^{\text{th}}$ grid-point ($\mathfrak{j} = 1,2, \ldots, \mathfrak{n}_{\mathfrak{r}}$), whereas $\mathfrak{n}_{\mathfrak{r}}$ is

the total number of grid-points. $\mathbb{a}_{ij}^{(\mathfrak{p})}$ for $i \neq \mathfrak{j}$ will be obtained by using Eq. (18) as [31].

$$\mathbb{a}_{\mathfrak{s}\mathfrak{j}}^{(\mathfrak{p})} = n\left(\mathbb{a}_{\mathfrak{s}\mathfrak{s}}^{(\mathfrak{p}-1)}\mathbb{a}_{\mathfrak{s}\mathfrak{j}}^{(1)} - \frac{\mathbb{a}_{\mathfrak{s}\mathfrak{j}}^{(\mathfrak{p}-1)}}{\mathfrak{r}_{\mathfrak{s}}-\mathfrak{r}_{\mathfrak{j}}}\right), \mathfrak{p} = 2,3,\ldots,\mathfrak{n}_{\mathfrak{r}}-1 and\ \mathfrak{s},\mathfrak{j} = 1,2,\ldots,\mathfrak{n}_{\mathfrak{r}}, \tag{18}$$

Here, the following connection [31] would construct $A_{\mathfrak{s}\mathfrak{j}}^{(1)}$.

$$\mathbb{a}_{\mathfrak{s}\mathfrak{j}}^{(1)} = \frac{\mathfrak{m}^{(1)}(\mathfrak{r}_{\mathfrak{s}})}{(\mathfrak{r}_{\mathfrak{s}}-\mathfrak{r}_{\mathfrak{j}})\mathfrak{m}^{(1)}(\mathfrak{r}_{\mathfrak{j}})}, \mathfrak{s},\mathfrak{j} = 1,2,\ldots,\mathfrak{n}_{\mathfrak{r}}, \tag{19}$$

The next relationship would be used to get $\mathcal{A}_{\mathfrak{s}\mathfrak{j}}^{(\mathfrak{p})}$.

$$\mathbb{a}_{\mathfrak{s}\mathfrak{s}}^{(\mathfrak{p})} = -\sum_{\mathfrak{j}=1,\mathfrak{j}\neq\mathfrak{s}}^{\mathfrak{n}_{\mathfrak{r}}}\mathbb{a}_{\mathfrak{s}\mathfrak{j}}^{(\mathfrak{p})}, \mathfrak{s} = 2,3,\ldots,\mathfrak{n}_{\mathfrak{r}}\ and\ \mathfrak{p} = 1,2,\ldots,\mathfrak{n}_{\mathfrak{r}}-1, \tag{20}$$

In Eq. (19), $\mathfrak{m}^{(1)}$ may be obtained as

$$\mathfrak{m}^{(1)}(\mathfrak{r}_k) = -\sum_{\mathfrak{j}=1,\mathfrak{j}\neq\mathfrak{f}}^{\mathbb{m}_{\mathfrak{r}}}\left(\mathfrak{r}_{\mathfrak{f}}-\mathfrak{r}_{\mathfrak{j}}\right), for\ \mathfrak{f} = 1,2,3,\ldots,\mathfrak{n}_{\mathfrak{r}}. \tag{21}$$

3.2 Two-dimensional approximation

The DQA's principles may be used to generate the first and second derivatives of a function such as $\sigma\ (\mathfrak{r},\theta)$ as follows [32]:

$$\left.\frac{\partial\sigma}{\partial\mathfrak{r}}\right|_{\mathfrak{r}=\mathfrak{r}_{\mathfrak{s}},\theta=\theta_{\mathfrak{j}}} = \sum_{\mathfrak{p}=1}^{\mathfrak{n}_{\mathfrak{r}}}\sum_{\mathfrak{f}=1}^{\mathfrak{n}_{\theta}}\mathbb{a}_{\mathfrak{s}\mathfrak{p}}^{\mathfrak{r}}I_{\mathfrak{p}\mathfrak{f}}^{\theta}\sigma_{\mathfrak{f}\mathfrak{j}}, \tag{22a}$$

$$\left.\frac{\partial\sigma}{\partial\theta}\right|_{\mathfrak{r}=\mathfrak{r}_{\mathfrak{s}},\theta=\theta_{\mathfrak{j}}} = \sum_{\mathfrak{p}=1}^{\mathfrak{n}_{\mathfrak{r}}}\sum_{\mathfrak{f}=1}^{\mathfrak{n}_{\theta}}I_{\mathfrak{s}\mathfrak{p}}^{\mathfrak{r}}\mathbb{a}_{\mathfrak{p}\mathfrak{f}}^{\theta}\sigma_{\mathfrak{f}\mathfrak{j}}, \tag{22b}$$

$$\frac{\partial}{\partial\mathfrak{r}}\left(\left.\frac{\partial\sigma}{\partial\theta}\right|_{\mathfrak{r}=\mathfrak{r}_{\mathfrak{s}},\theta=\theta_{\mathfrak{j}}}\right) = \sum_{\mathfrak{p}=1}^{\mathfrak{n}_{\mathfrak{r}}}\sum_{\mathfrak{f}=1}^{\mathfrak{n}_{\theta}}\mathbb{a}_{\mathfrak{s}\mathfrak{p}}^{\mathfrak{r}}\mathbb{a}_{\mathfrak{p}\mathfrak{f}}^{\theta}\sigma_{\mathfrak{f}\mathfrak{j}}, \tag{22c}$$

$$\left.\frac{\partial^2\sigma}{\partial\mathfrak{r}^2}\right|_{\mathfrak{r}=\mathfrak{r}_{\mathfrak{s}},\theta=\theta_{\mathfrak{j}}} = \sum_{\mathfrak{p}=1}^{\mathfrak{n}_{\mathfrak{r}}}\sum_{\mathfrak{f}=1}^{\mathfrak{n}_{\theta}}\mathbb{b}_{\mathfrak{s}\mathfrak{p}}^{\mathfrak{r}}I_{\mathfrak{p}\mathfrak{f}}^{\theta}\sigma_{\mathfrak{f}\mathfrak{j}}, \tag{22d}$$

$$\left.\frac{\partial^2\sigma}{\partial\theta^2}\right|_{\mathfrak{r}=\mathfrak{r}_{\mathfrak{s}},\theta=\theta_{\mathfrak{j}}} = \sum_{\mathfrak{p}=1}^{\mathfrak{n}_{\mathfrak{r}}}\sum_{\mathfrak{f}=1}^{\mathfrak{n}_{\theta}}I_{\mathfrak{s}\mathfrak{p}}^{\mathfrak{r}}\mathbb{b}_{\mathfrak{p}\mathfrak{f}}^{\theta}\sigma_{\mathfrak{f}\mathfrak{j}}. \tag{22e}$$

In this case, the equivalent weight coefficients are $\mathbb{a}_{\mathfrak{p}\mathfrak{f}}^{\theta}$, $\mathbb{a}_{i\mathfrak{p}}^{\mathfrak{r}}$, $\mathbb{b}_{\mathfrak{p}\mathfrak{f}}^{\theta}$, and $\mathbb{b}_{i\mathfrak{p}}^{\mathfrak{r}}$. Additionally, the number of discrete grid points in the radial and circumferential directions is represented by $\mathfrak{n}_{\theta}$, and $\mathfrak{n}_{\mathfrak{r}}$. $I_{i\mathfrak{p}}^{\mathfrak{r}}$, $I_{\mathfrak{p}\mathfrak{f}}^{\theta}$, $I_{i\mathfrak{p}}^{\mathfrak{r}}$, and $I_{\mathfrak{p}\mathfrak{f}}^{\theta}$ should be considered identity tensors. The following polar coordination of $(\mathfrak{r}_i,\theta_{\mathfrak{j}})$ may be established as the grid-point representation using the Chebyshev-Gauss-Lobatto function [31]:

$$\mathfrak{r}_z = \mathfrak{r}_i + \frac{\mathfrak{r}_o-\mathfrak{r}_i}{2}\left(1 - cos\left(\frac{(\mathfrak{s}-1)}{(\mathfrak{n}_{\mathfrak{r}}-1)}\pi\right)\right)\mathfrak{s} = 1,2,3,\ldots,\mathfrak{n}_{\mathfrak{r}}, \tag{23a}$$

$$\theta_{\mathfrak{j}} = \frac{\theta}{2}\left(1 - cos\left(\frac{(\mathfrak{j}-1)}{(\mathfrak{n}_\theta - 1)}\pi\right)\right) \mathfrak{j} = 1,2,3,\ldots,\mathfrak{n}_\theta. \tag{23b}$$

The following relations result from using the Laplace transform [33] after inserting Eqs. (22a-e) and (16) in Eqs. (14a-l) and using Eq. (15).

$$\begin{bmatrix} \mathbb{K}_{11} + \mathbb{M}_{11}S^2 & \cdots & \mathbb{K}_{112} + \mathbb{M}_{112}S^2 \\ \vdots & \ddots & \vdots \\ \mathbb{K}_{121} + \mathbb{M}_{121}S^2 & \cdots & \mathbb{K}_{1212} + \mathbb{M}_{1212}S^2 \end{bmatrix} [\mathbb{X}]^T = [\mathbb{F}]^T. \tag{24}$$

where

$$[\mathbb{X}] = [\mathfrak{u}_0 \quad \mathfrak{v}_0 \quad \mathfrak{w}_0 \quad \mathfrak{u}_1 \quad \mathfrak{v}_1], \tag{25a}$$

$$[\mathbb{F}] = [0 \quad 0 \quad PH(t - t_0) \quad 0 \quad 0], \tag{25b}$$

$$P = \{P_1, \ldots\ldots, P_{\mathfrak{n}_r \times \mathfrak{n}_\theta}\}^T. \tag{25c}$$

Layer-wise displacements are produced by applying the Laplace transform to Eq. (24) and then substituted into Eq. (7) to calculate stresses. The stress and displacement distributions along the thickness of the plate are therefore given by Eq. (9). The improved Dubner-Abate approach, represented in Eq. (26), is used to recover time-dependent thermal and mechanical fields by inverting the Laplace transform.

$$f(t) = \frac{2e^{at}}{T}\left[-\frac{A_0}{2} + \sum_{\mathfrak{f}=0}^{\infty}\left(A_{\mathfrak{f}} cos\left(\frac{2\mathfrak{f}\pi t}{T}\right) - B_{\mathfrak{f}} sin\left(\frac{2\mathfrak{f}\pi t}{T}\right)\right)\right], \tag{26}$$

Here

$$A_0 = Re[\mathbb{F}(a)], A_{\mathfrak{f}} = Re\left[\mathbb{F}\left(a + i\frac{2\mathfrak{f}\pi}{T}\right)\right], B_{\mathfrak{f}} = Im\left[\mathbb{F}\left(a + i\frac{2\mathfrak{f}\pi}{T}\right)\right],$$
$$S = a + i\frac{2\mathfrak{f}\pi}{T}, aT = 5. \tag{27}$$

Dimensionless amounts are also defined by

$$(\bar{u}_r \quad \bar{u}_\theta \quad \bar{u}_z) = \frac{1}{h}(\mathfrak{u} \quad \mathfrak{v} \quad \mathfrak{w}),$$
$$\bar{\mathfrak{r}} = \frac{\mathfrak{r}}{R_m}, \bar{\mathfrak{z}} = \frac{\mathfrak{z}}{h}, \quad \bar{\mathfrak{P}}_{ij} = \frac{\mathfrak{P}_{ij}}{P_0}, \bar{P} = \frac{\mathfrak{p}}{P_0}, P_0 = 1[\mathbb{m}Pa]. \tag{28}$$

4. Results and discussion:

4.1 Verification study

Table 1 provides a comparative analysis of stresses and dimensionless displacements for a functionally graded graphene platelet-reinforced composite multilayer annular plate subjected to a cosinusoidal load. The results are evaluated under two distinct boundary conditions, namely clamped–simply supported–clamped–simply supported (CSCS) and simply supported on all edges (SSSS), and are compared with previously reported data (Ref. [34]) to validate the present

Table 1. Comparing the dimensionless center deflections of a square functionally graded plate under a constant load

Boundary conditions		$\mathfrak{w}/h$	$\mathfrak{v}/h$	$\mathfrak{u}/h$
CSCS	Ref. [34]	−14.010	0.4859	−0.1891
	Present	−14.007	0.4853	−0.1887
SSSS	Ref. [34]	−36.154	−0.2284	0.7076
	Present	−36.150	−0.2281	0.7075

formulation. The parameters $\mathfrak{w}/h$, $\mathfrak{v}/h$, and $\mathfrak{u}/h$ represent the normalized transverse, circumferential, and radial displacements, respectively. Under CSCS boundary conditions, the results demonstrate a close agreement between the reference and present values. Specifically, the transverse displacement $\mathfrak{w}/h$ shows a negligible difference (−14.010 vs. −14.007), while similarly minor deviations are observed for $\mathfrak{v}/h$ and $\mathfrak{u}/h$. This consistency confirms the accuracy and reliability of the current semi-analytical model. A comparable trend is observed for the SSSS boundary condition. The transverse displacement $\mathfrak{w}/h$ and in-plane displacements $\mathfrak{v}/h$ and $\mathfrak{u}/h$ exhibit minimal discrepancies between the reference and present results. Notably, the magnitude of deformation under SSSS conditions is significantly higher than that of CSCS, indicating reduced structural stiffness due to less restrictive boundary constraints. Overall, the strong correlation between the present results and established data validates the effectiveness of the adopted modeling approach. Furthermore, the sensitivity of displacement responses to boundary conditions highlights the importance of support configurations in the mechanical performance of FG-GPLRC annular plates under dynamic loading.

4.2 Parametric results

Table 2 presents a comparative evaluation of the influence of GPL geometry on reinforcement efficiency and fabrication cost within composite materials. Five geometrical configurations, square, rectangular, circular, irregular, and triangular, are assessed across multiple performance indicators, including mechanical reinforcement efficiency, load transfer area, stress concentration level, dispersion quality, and relative fabrication cost. Rectangular GPLs exhibit the highest reinforcement efficiency, particularly along their longitudinal direction, due to their extended aspect ratio, which enhances load transfer capability. This geometry also provides a very high load transfer area and very good dispersion quality, while maintaining a relatively low-to-medium fabrication cost, making it highly favorable for engineering applications. Square GPLs demonstrate balanced performance, offering high reinforcement efficiency and good dispersion, with moderate stress concentration and cost. Circular GPLs, while exhibiting excellent dispersion quality due to their isotropic shape, show only medium reinforcement efficiency and relatively high fabrication cost. Their low stress concentration, however, can be advantageous in reducing failure risks. In contrast, irregular GPLs present variable dispersion quality and lower reinforcement efficiency but benefit from very low fabrication costs, suggesting suitability for cost-sensitive applications despite performance trade-offs. Triangular GPLs provide moderate reinforcement and load transfer characteristics but are associated with higher stress concentration levels and medium-to-high fabrication costs. Overall, the table highlights that GPL geometry plays a critical role in balancing mechanical performance and economic feasibility in composite design.

Table 2. Influence of GPL geometry on reinforcement efficiency and cost

GPL Geometry	Mechanical Reinforcement Efficiency	Load Transfer Area	Stress Concentration Level	Dispersion Quality	Relative Fabrication Cost
Square	High	High	Medium	Good	Medium
Rectangular	Very high in the long direction	Very high	Medium–High	Very good	Low–Medium
Circular	Medium	Medium–High	Low	Excellent	High
Irregular	Low–Medium	Low–Medium	High	Variable	Very Low
Triangular	Medium	Medium	High	Good	Medium–High

Table 3. The best and optimized geometry for graphene nanoplatelets in most structural and multifunctional composite applications

Large lateral size	20 μm
Type of GPL distribution pattern	GPL-X
Moderate width	5 μm
Thin thickness	5 nm
Aspect ratio	3000

Based on the comparison of geometrical characteristics, reinforcement efficiency, dispersion behavior, and fabrication cost, the best and optimized geometry for graphene nanoplatelets in most structural and multifunctional composite applications is presented in Table 3.

So, using the values of Table 3, the following results are obtained. These values are optimal because, maximizes load transfer and stiffness enhancement, maintains good dispersion stability, offers low-to-moderate fabrication cost, provides excellent directional reinforcement for laminated and functionally graded composites, matches well with semi-analytical optimization models due to predictable shape and behavior.

4.2.1 Deflection analysis

Fig. 1 illustrates the variation of deflection along the thickness direction of the annular plate structure for different values of the angle of the annular plate. The horizontal axis represents the normalized position along the thickness direction, while the vertical axis denotes the corresponding deflection. Three cases of angular configuration are considered, showing a clear linear distribution of deflection across the thickness. The results demonstrate that increasing the angle of the annular plate significantly amplifies the magnitude of deflection. Specifically, the configuration with the largest angular value produces the steepest gradient, indicating higher deformation sensitivity through the thickness. This behavior can be attributed to the geometric influence of the plate angle on stiffness characteristics, where larger angles reduce effective resistance to deformation under loading. The symmetric nature of the deflection distribution about the mid-thickness confirms the consistency of the mechanical model based on first-order shear deformation theory, which captures transverse shear effects while maintaining linear variation assumptions. Additionally, the intersection point at the mid-thickness indicates a neutral plane where deflection transitions from compressive to tensile behavior. From a design perspective, the figure highlights the importance of controlling the angle of the annular plate in optimizing structural performance. Smaller angles result in reduced deformation, which is beneficial for applications requiring higher stiffness and dimensional

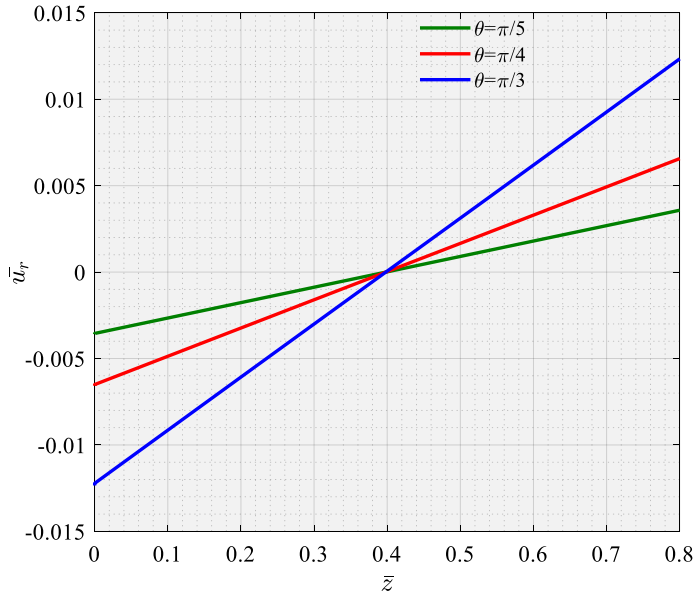

Figure 1. The variation of deflection along the thickness direction of the annular plate structure for different values of the angle of the annular plate

stability. Conversely, larger angles may be advantageous in applications where flexibility or energy absorption under shock loading is desired.

Fig. 2 presents the effect of varying the outer radius of the annular plate structure relative to the inner radius of the annular plate structure on the deflection distribution along the thickness direction. The results show a linear variation of deflection across the thickness, consistent with the assumptions of the semi-analytical formulation. As the outer radius of the annular plate structure increases, a noticeable rise in the magnitude of deflection is observed. Larger outer radius values lead to a greater structural span, which reduces the overall stiffness of the system and increases its susceptibility to deformation under external shock excitation. This trend is clearly reflected in the steeper slope of the deflection profile for higher radius ratios. The midpoint along the thickness direction remains the neutral surface, where deflection transitions between compressive and tensile regions. This indicates that the structural behavior remains mechanically consistent despite geometric variations. From a physical standpoint, increasing the outer radius effectively enhances bending moments induced by the external shock excitation, thereby amplifying deformation. This highlights a critical trade-off in design: while larger geometries may be required for functional or spatial reasons, they can compromise structural rigidity. In the context of graphene nanoplatelet-reinforced composites, this figure emphasizes the necessity of optimizing geometric parameters alongside material reinforcement. Proper selection of the outer radius of the annular plate structure can significantly influence performance, particularly in applications subjected to dynamic or shock loading conditions.

Fig. 3 examines the influence of varying levels of external shock excitation on the deflection distribution along the thickness direction of the annular plate structure. The horizontal axis represents the position along the thickness direction, while the vertical axis shows the corresponding deflection. The results indicate a direct and proportional relationship between the magnitude of

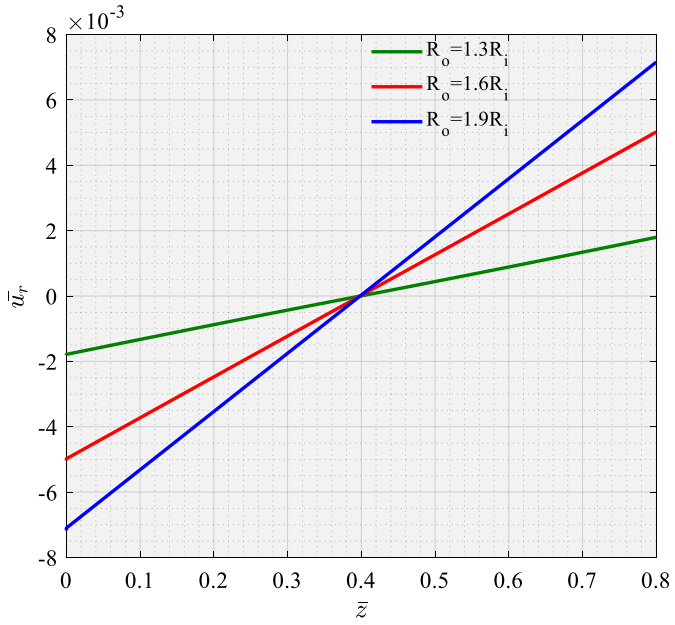

Figure 2. The effect of varying the outer radius of the annular plate structure relative to the inner radius of the annular plate structure on the deflection distribution along the thickness direction

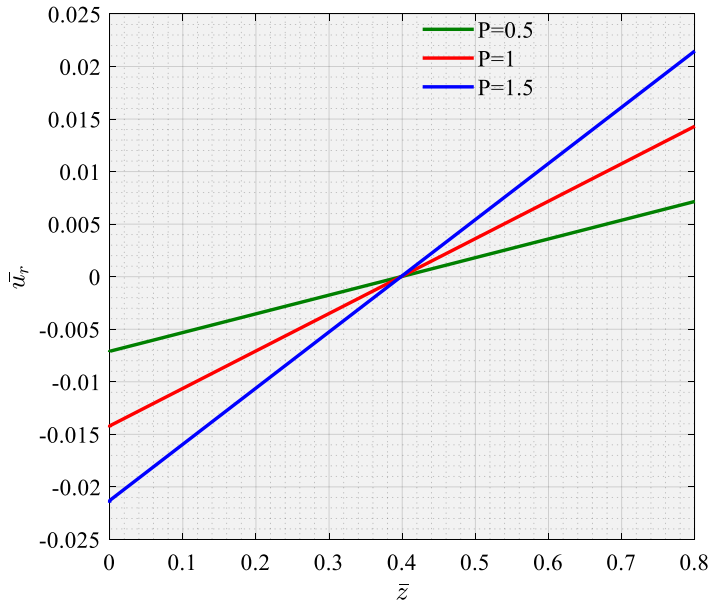

Figure 3. The influence of varying levels of external shock excitation on the deflection distribution along the thickness direction of the annular plate structure

external shock excitation and the resulting deflection. As the intensity of the applied shock increases, the slope of the deflection curve becomes steeper, indicating higher deformation throughout the

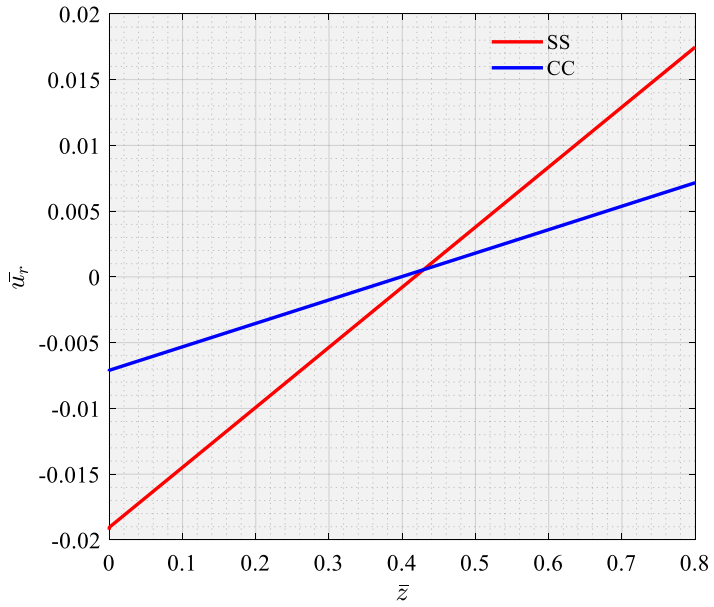

Figure 4. The deflection distribution along the thickness direction for two different boundary conditions

thickness. This linear scaling behavior confirms the stability and consistency of the semi-analytical solution approach. The symmetry of the curves about the mid-thickness suggests that the mechanical response remains uniform and predictable, with a well-defined neutral plane. This behavior aligns with the governing assumptions of first-order shear deformation theory, where transverse shear effects are incorporated without introducing nonlinearities in the thickness-wise response. From an engineering perspective, this figure highlights the critical role of external shock excitation in determining structural performance. Higher shock loads significantly increase deformation, which may lead to structural failure if not properly accounted for in design. The incorporation of graphene nanoplatelets can mitigate this effect by enhancing stiffness and energy absorption capacity. Therefore, optimizing both the reinforcement geometry and the expected loading conditions is essential for achieving a balance between mechanical reliability and cost-effective material usage.

Fig. 4 compares the deflection distribution along the thickness direction for two different boundary conditions: simply supported and clamped supported configurations. The horizontal axis represents the position along the thickness direction, while the vertical axis indicates deflection. The results reveal that the simply supported condition produces significantly higher deflection compared to the clamped supported condition. This difference arises because clamped supports restrict both displacement and rotation at the boundaries, thereby increasing structural stiffness and reducing deformation. In contrast, simply supported boundaries allow rotational freedom, resulting in greater flexibility and higher deflection under the same loading conditions. Both cases exhibit a linear variation of deflection across the thickness, with a neutral plane located at the mid-thickness. However, the slope of the deflection curve is noticeably steeper for the simply supported configuration, indicating a more pronounced response to loading. This comparison underscores the importance of boundary conditions in structural design. The selection of support type can significantly influence the overall mechanical behavior of the annular plate structure, particularly

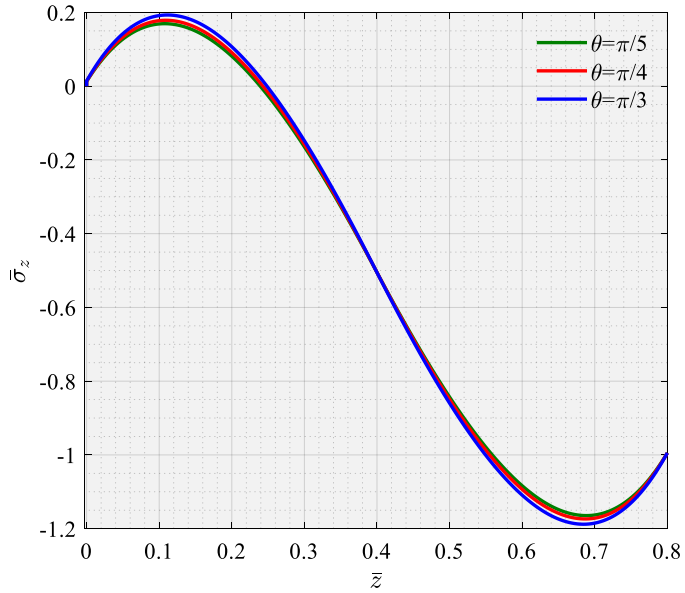

Figure 5. The variation of normal stress along the thickness direction of the annular plate for different angular positions of the structure

under external shock excitation. In practical applications, clamped supports are preferred when minimizing deformation is critical, such as in high-precision or load-bearing systems. Conversely, simply supported configurations may be suitable where flexibility and ease of fabrication are prioritized. The integration of graphene nanoplatelet reinforcements further enhances the ability to tailor structural performance under different boundary constraints.

4.2.2 Normal stress

Fig. 5 illustrates the variation of normal stress along the thickness direction of the annular plate for different angular positions of the structure. The horizontal axis represents the coordinate along the thickness direction, while the vertical axis denotes the normal stress. The results clearly show that the angular position of the annular plate has a noticeable yet moderate influence on the stress distribution through the thickness. For all considered angular configurations, the stress profile follows a nonlinear pattern, initially increasing to a maximum positive value near the upper surface and then decreasing sharply toward the lower surface, where compressive stresses dominate. As the angular position increases, slight deviations in the magnitude of both tensile and compressive stresses are observed. Specifically, higher angular values tend to slightly increase the peak tensile stress while also marginally affecting the location and depth of the compressive region. However, the overall trend remains consistent, indicating that the structural response is relatively stable with respect to angular variation. From a physical standpoint, this behavior can be attributed to the redistribution of internal forces caused by geometric orientation under external shock excitation. Within the framework of graphene nanoplatelet-reinforced composites, this suggests that angular positioning does not drastically compromise structural integrity but can be fine-tuned to optimize performance. Consequently, the figure highlights that angular design can be considered a secondary optimization parameter in achieving balanced stress distribution and cost-effective fabrication.

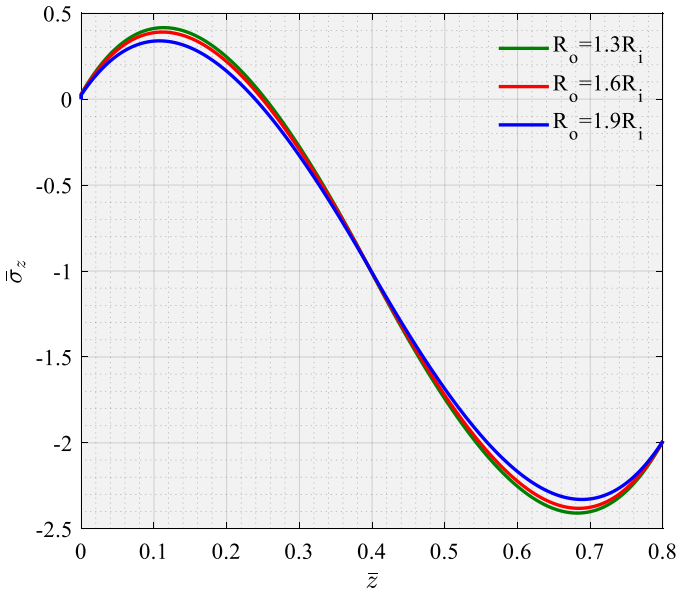

Figure 6. The influence of the ratio between the outer radius and inner radius of the annular plate on the normal stress distribution along the thickness direction

Fig. 6 presents the influence of the ratio between the outer radius and inner radius of the annular plate on the normal stress distribution along the thickness direction. The results demonstrate that geometric scaling of the annular plate significantly affects the magnitude and distribution of stress under external shock excitation. As the outer radius increases relative to the inner radius, the structure becomes more flexible, which leads to higher stress magnitudes, particularly in the compressive region near the lower surface. The stress profiles reveal that all configurations follow a similar nonlinear trend; however, the amplitude of stress variation increases with larger radius ratios. Specifically, a larger outer radius intensifies both tensile and compressive stresses due to the increased bending moment and structural deformation. This indicates that the geometric proportion of the annular plate plays a critical role in determining its resistance to dynamic loading. From the perspective of graphene nanoplatelet reinforcement optimization, this finding is highly significant. Increasing the size of the structure may enhance certain functional requirements, but it also raises stress levels, which could demand higher material strength or increased reinforcement. Therefore, a balance must be achieved between geometric design and material cost. Overall, this figure emphasizes that the ratio of outer radius to inner radius is a dominant design parameter that directly influences mechanical performance and fabrication efficiency, making it a key factor in the proposed semi-analytical optimization framework.

Fig. 7 examines the impact of different levels of external shock excitation on the normal stress distribution along the thickness direction of the annular plate. The horizontal axis corresponds to the thickness coordinate, while the vertical axis represents the normal stress. The results clearly indicate that increasing the magnitude of external shock excitation leads to a substantial amplification of stress throughout the structure. At lower levels of external shock excitation, the stress distribution remains relatively moderate, with limited variation between tensile and compressive regions. However, as the intensity of the applied shock increases, both the peak

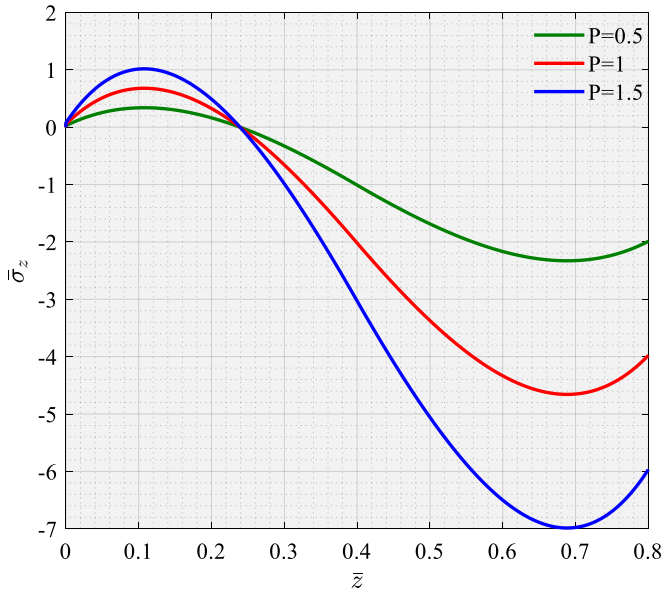

Figure 7. The impact of different levels of external shock excitation on the normal stress distribution along the thickness direction of the annular plate

tensile stress near the upper surface and the compressive stress near the lower surface grow significantly. This demonstrates a strong nonlinear relationship between loading intensity and structural response. The figure also shows that higher shock levels result in a steeper stress gradient across the thickness, indicating increased susceptibility to material failure or delamination, particularly in composite structures reinforced with graphene nanoplates. This highlights the importance of accurately predicting dynamic responses when designing such advanced materials. From an optimization standpoint, this behavior underscores the necessity of tailoring graphene nanoplatelet geometry and distribution to withstand varying levels of shock loading. While stronger reinforcement can improve resistance, it may also increase fabrication cost. Therefore, the figure supports the study's objective of balancing mechanical performance with economic considerations.

Fig. 8 compares the influence of different boundary conditions, specifically simply supported and clamped supports, on the normal stress distribution along the thickness direction. The results demonstrate that boundary conditions play a crucial role in determining the structural response of the annular plate under external shock excitation. In the simply supported configuration, the stress distribution is smoother and more gradual, indicating greater flexibility in deformation. This leads to lower peak stresses compared to the clamped condition. In contrast, the clamped configuration restricts displacement at the boundaries, resulting in higher stiffness and consequently larger stress concentrations, particularly in the compressive region near the lower surface. The difference between the two conditions becomes more pronounced as the thickness coordinate approaches the lower surface, where the clamped structure exhibits significantly higher compressive stress. This suggests that while clamped supports can enhance overall rigidity, they may also increase the risk of localized failure due to stress concentration. From the perspective of graphene nanoplatelet-reinforced composite design, this finding is highly relevant. The choice of boundary condition

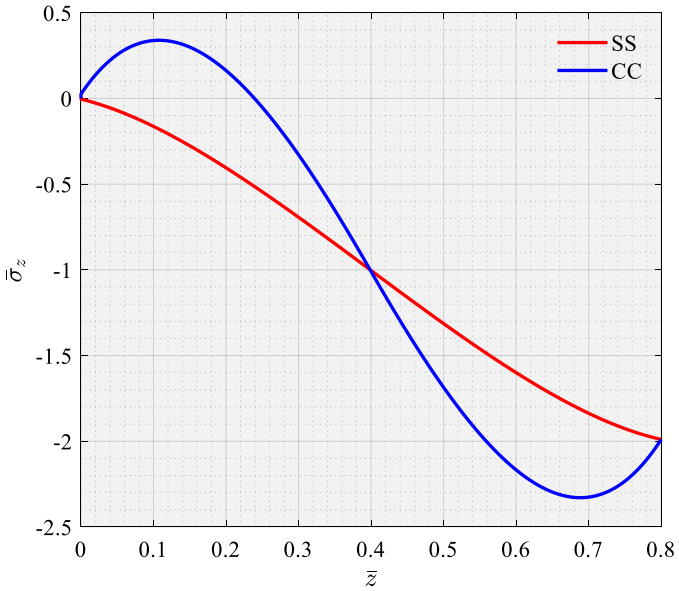

Figure 8. The influence of different boundary conditions, specifically simply supported and clamped supports, on the normal stress distribution along the thickness direction

directly affects the required level of reinforcement and, consequently, the fabrication cost. A clamped structure may require more advanced reinforcement strategies to mitigate high stresses, whereas a simply supported design may allow for more economical material usage. Overall, this figure highlights the critical role of support conditions in the optimization process, reinforcing their importance in achieving an efficient balance between mechanical performance and manufacturing cost.

5. Conclusion

This study has presented a comprehensive semi-analytical framework for optimizing the geometry of graphene nanoplatelet reinforcements while effectively managing fabrication costs in advanced composite structures subjected to external shock loading. The integration of the Halpin–Tsai model has enabled accurate estimation of the effective material properties, capturing the influence of nanoplatelet geometry, aspect ratio, and dispersion patterns. The adoption of FSDT has ensured reliable representation of transverse shear effects, particularly in moderately thick composite plates. Hamilton's principle has been successfully employed to derive the governing equations of motion, providing a rigorous foundation for analyzing the dynamic response under transient shock excitation. The DQM has been utilized as an efficient semi-analytical solution technique, offering high accuracy with reduced computational complexity. Furthermore, the application of the Laplace transform method has facilitated stable and precise treatment of time-dependent loading conditions. The investigation has systematically evaluated the role of GNP geometry in enhancing structural performance, demonstrating that optimized configurations have significantly improved stiffness, strength, and shock resistance. At the same time, the study has

established that careful control of nanoplatelet distribution and aspect ratio has contributed to minimizing material usage and simplifying fabrication processes. As a result, an effective balance between mechanical performance and cost efficiency has been achieved. Overall, the proposed methodology has provided a robust and scalable tool for the design and optimization of graphene-reinforced composite systems. The findings have contributed valuable insights into the interplay between reinforcement geometry, dynamic behavior, and manufacturing considerations. This work has laid a solid foundation for future research aimed at extending the approach to more complex loading scenarios, multi-scale modeling, and industrial-scale applications.

Acknowledgment

This research is funded by Zarqa University.

References

1. Adab, N., Arefi, M. (2023). Vibrational behavior of truncated conical porous GPL-reinforced sandwich micro/nano-shells. Engineering with Computers, 39(1), 419-443. https://doi.org/10.1007/s00366-021-01595-1
2. Adab, N., Arefi, M., Amabili, M. (2022). A comprehensive vibration analysis of rotating truncated sandwich conical microshells including porous core and GPL-reinforced face-sheets. Composite Structures, 279, 114761. https://doi.org/10.1016/j.compstruct.2021.114761
3. Bahranifard, F., Golbahar Haghighi, M.R., Malekzadeh, P. (2020). In-plane responses of multilayer FG-GPLRC curved beams in thermal environment under moving load. Acta Mechanica, 231(7), 2679-2696. https://doi.org/10.1007/s00707-020-02663-1
4. Barati, M.R., Zenkour, A.M. (2019). Analysis of postbuckling of graded porous GPL-reinforced beams with geometrical imperfection. Mechanics of Advanced Materials and Structures, 26(6), 503-511. https://doi.org/10.1080/15376494.2017.1410918
5. Barati, M.R., Zenkour, A.M. (2019). Analysis of postbuckling of graded porous GPL-reinforced beams with geometrical imperfection. Mechanics of Advanced Materials and Structures, 26(6), 503-511. https://doi.org/10.1080/15376494.2017.1410918
6. Bo, L., Li, Q., Tian, Y., Wu, D., Yu, Y., Chen, X., Gao, W. (2022). Nonlinear dynamic investigation of the perovskite solar cell with GPLR-FGP stiffeners under blast impact. International Journal of Mechanical Sciences, 213, 106866. https://doi.org/10.1016/j.ijmecsci.2021.106866
7. Bidzard, A., Malekzadeh, P., Mohebpour, S.R. (2022). A size-dependent nonlinear finite element free vibration analysis of multilayer FG-GPLRC toroidal micropanels in thermal environment. Composite Structures, 279, 114783. https://doi.org/10.1016/j.compstruct.2021.114783
8. Dat, N.D., Anh, V.T.T., Duc, N.D. (2023). Vibration characteristics and shape optimization of FG-GPLRC cylindrical shell with magneto-electro-elastic face sheets. Acta Mechanica, 234(9), 4749-4773. https://doi.org/10.1007/s00707-023-03621-3
9. Ghadiri Rad, M.H., Hosseini, S.M. (2022). Application of the CUF-EFG method for buckling analysis of the multilayer GPLs-CNTs-reinforced FG plates with cutout. Mechanics of Advanced Materials and Structures, 29(27), 1-17. https://doi.org/10.1080/15376494.2022.2077158
10. Ghadiri Rad, M.H., Hosseini, S.M. (2024). A new coupled meshless method based on the CUF and MLPG method for dynamic analysis of thick multilayer FG GPLs-CNTs reinforced composite plates. Mechanics of Advanced Materials and Structures, 31(26), 1-20. https://doi.org/10.1080/15376494.2022.2162669
11. Jayakumari, B.Y., Swaminathan, E.N., Partheeban, P. (2024). Sustainable construction material using

nanosilica and multi-walled carbon nanotubes in cement concrete. Advances in Nano Research, 16(5), 459-472. https://doi.org/10.12989/anr.2024.16.5.459
12. Duc, L.B., Le, B.T., Quoc, K.D., Tran, T.B., Singh, R. (2025). Investigation the effects of compaction pressure and sintering temperature on mechanical properties of Al-x% TiC composite. Advances in Materials Research, 14(1), 71-79. https://doi.org/10.12989/amr.2025.14.1.071
13. Zouatnia, N., Hadji, L. (2019). Static and free vibration behavior of functionally graded sandwich plates using a simple higher order shear deformation theory. Advances in Materials Research, 8(4), 313-335. https://doi.org/10.12989/amr.2019.8.4.313
14. Ahlawat, N., Saini, R. (2024). Vibration and buckling analysis of elastically supported Bi-directional FGM mindlin circular plates having variable thickness. Journal of Vibration Engineering & Technologies, 12(1), 513-532. https://doi.org/10.1007/s42417-023-00860-5
15. Alijani, F., Amabili, M., Ferrari, G., D'Alessandro, V. (2013). Nonlinear vibrations of laminated and sandwich rectangular plates with free edges. Part 2: Experiments & comparisons. Composite Structures, 105, 437-445. https://doi.org/10.1016/j.compstruct.2013.06.004
16. Kumar, Y., Gupta, A., Tounsi, A. (2021). Size-dependent vibration response of porous graded nanostructure with FEM and nonlocal continuum model. Advances in Nano Research, 11(1), 1-17. https://doi.org/10.12989/anr.2021.11.1.001
17. Hajmohammad, M.H., Zarei, M.S., Farrokhian, A., Kolahchi, R. (2018). A layerwise theory for buckling analysis of truncated conical shells reinforced by CNTs and carbon fibers integrated with piezoelectric layers in hygrothermal environment. Advances in Nano Research, 6(4), 299-321. https://doi.org/10.12989/anr.2018.6.4.299
18. Djebbour, K.D., Nebab, M., Avcar, M., Ait Atmane, H., Bernard, F., Bennai, R., Ikinci, B. (2025). Stability and vibration analysis of shear deformable FG-CNTRC beams resting on elastic foundations. Advances in Nano Research, 18(3), 205-221. https://doi.org/10.12989/anr.2025.18.3.205
19. Shen, X., Li, T., Xu, L., Kiarasi, F., Babaei, M., Asemi, K. (2024). Free vibration analysis of FG porous spherical cap reinforced by graphene platelet resting on Winkler foundation. Advances in Nano Research, 16(1), 11-26. https://doi.org/10.12989/anr.2024.16.1.011
20. Avcar, M., Hadji, L., Civalek, O. (2023). The influence of non-linear carbon nanotube reinforcement on the natural frequencies of composite beams. Advances in Nano Research, 14(5), 421-433. https://doi.org/10.12989/anr.2023.14.5.421
21. Liu, B., Wang, Y., Rabczuk, T., Olofsson, T., Lu, W. (2024). Multi-scale modeling in thermal conductivity of Polyurethane incorporated with Phase Change Materials using Physics-Informed Neural Networks. Renewable Energy, 220, 119565. https://doi.org/10.1016/j.renene.2023.119565
22. Bie, Y., Ren, H., Bui, T.Q., Madenci, E., Rabczuk, T., Wei, Y. (2024). Dual-horizon peridynamics modeling of coupled chemo-mechanical-damage for interface oxidation-induced cracking in thermal barrier coatings. Computer Methods in Applied Mechanics and Engineering, 430, 117225. https://doi.org/10.1016/j.cma.2024.117225
23. Guo, H., Zhuang, X., Rabczuk, T. (2021). A deep collocation method for the bending analysis of Kirchhoff plate. arXiv preprint arXiv:2102.02617. https://doi.org/10.48550/arXiv.2102.02617
24. Zhuang, X., Guo, H., Alajlan, N., Zhu, H., Rabczuk, T. (2021). Deep autoencoder based energy method for the bending, vibration, and buckling analysis of Kirchhoff plates with transfer learning. European Journal of Mechanics - A/Solids, 87, 104225. https://doi.org/10.1016/j.euromechsol.2021.104225
25. Samaniego, E., Anitescu, C., Goswami, S., Nguyen-Thanh, V.M., Guo, H., Hamdia, K., Zhuang, X., Rabczuk, T. (2020). An energy approach to the solution of partial differential equations in computational mechanics via machine learning: Concepts, implementation and applications. Computer Methods in Applied Mechanics and Engineering, 362, 112790. https://doi.org/10.1016/j.cma.2019.112790
26. Carrera, E., Scano, D. (2023). Finite elements based on Jacobi shape functions for the free vibration analysis of beams, plates, and shells. Mechanics of Advanced Materials and Structures, 30(8), 1-9. https://doi.org/10.1080/15376494.2021.2023928

27. Carrera, E., Zozulya, V.V. (2022). Carrera unified formulation (CUF) for the micropolar plates and shells. I. Higher order theory. Mechanics of Advanced Materials and Structures, 29(4), 773-795. https://doi.org/10.1080/15376494.2020.1833115
28. Carrera, E., Zozulya, V.V. (2022). Carrera unified formulation for the micropolar plates. Mechanics of Advanced Materials and Structures, 29(19), 3163-3186. https://doi.org/10.1080/15376494.2021.1884913
29. Marin, M., Carrera, E., Vlase, S. (2023). An extension of the Hamilton variational principle for piezoelectric bodies with dipolar structure. Mechanics of Advanced Materials and Structures, 30(12), 2453-2457. https://doi.org/10.1080/15376494.2022.2052205
30. Yan, Y., Carrera, E., Pagani, A. (2022). Free vibration analysis of curved metallic and composite beam structures using a novel variable-kinematic DQ method. Mechanics of Advanced Materials and Structures, 29(22), 3743-3762. https://doi.org/10.1080/15376494.2021.1924359
31. Tornabene, F. (2009). Free vibration analysis of functionally graded conical, cylindrical shell and annular plate structures with a four-parameter power-law distribution. Computer Methods in Applied Mechanics and Engineering, 198(37-40), 2911-2935. https://doi.org/10.1016/j.cma.2009.04.011
32. Javani, M., Kiani, Y., Eslami, M.R. (2022). On the free vibrations of FG-GPLRC folded plates using GDQE procedure. Composite Structures, 286, 115273. https://doi.org/10.1016/j.compstruct.2022.115273
33. Nguyen, S.N., Cho, M., Kim, J.S., Han, J.W. (2022). Improved thermo-mechanical-viscoelastic analysis of laminated composite structures via the enhanced Lo-Christensen-Wu theory in the Laplace domain. Mechanics of Advanced Materials and Structures, 29(27), 7123-7139. https://doi.org/10.1080/15376494.2021.1992055
34. Liu, D., Li, Z., Kitipornchai, S., Yang, J. (2019). Three-dimensional free vibration and bending analyses of functionally graded graphene nanoplatelets-reinforced nanocomposite annular plates. Composite Structures, 229, 111453. https://doi.org/10.1016/j.compstruct.2019.111453